Renewable Energy 37 (2012) 285–298

Contents lists available at ScienceDirect

Renewable Energy

journal homepage: www.elsevier.com/locate/renene

Dynamic overset CFD simulations of wind turbine aerodynamics

Yuwei Li [a,1], Kwang-Jun Paik [a,2], Tao Xing [b,3], Pablo M. Carrica [c,*]

[a] IIHR-Hydroscience and Engineering, C. Maxwell Stanley Hydraulics Laboratory, The University of Iowa, Iowa City, IA 52242, USA
[b] Department of Mechanical Engineering, College of Engineering, University of Idaho, Moscow, ID 83844, USA
[c] Department of Mechanical and Industrial Engineering and IIHR-Hydroscience and Engineering, C. Maxwell Stanley Hydraulics Laboratory, The University of Iowa, Iowa City, IA 52242, USA

ARTICLE INFO

Article history:
Received 21 November 2010
Accepted 18 June 2011
Available online 18 July 2011

Keywords:
Wind turbine aerodynamics
Overset grids
Rotor flow
Computational fluid dynamics

ABSTRACT

Simulations of the National Renewable Energy Laboratory (NREL) phase VI wind turbine using dynamic overset grid technology are presented. The simulations are performed in an inertial frame of reference with the rotor consisting of the blades and hub. The geometries of the tower and nacelle are approximate but included in the computation. Computations of the effect of wind speed (5, 10, 15 and 25 m/s) at a fixed blade pitch angle of 3° with constant rotational speed using unsteady Reynolds-Averaged Navier–Stokes (RANS) and Detached Eddy Simulation (DES) turbulence models, both showing little difference in the averaged forces and moments. However, significant improvements in the transient response are seen when using DES. The effect of angle of attack is evaluated by dynamically changing the pitch from −15° to 40° at constant wind speed of 15 m/s. Extensive comparison against experimental results, including total power and thrust, sectional performance of normal force coefficient and local pressure coefficient, shows consistently good predictions. The methodology shows a promise for more complex computations including active turbine control by varying the pitch angle and fluid-structure interaction.

1. Introduction

Wind energy available around the world is much greater than the current world energy consumption. The generation potential of wind power on land and near off-shore is estimated at 72 TW, over five times the world's current energy use in all forms [1]. Predictions show that the global electric wind capacity will stand at 409 GW in 2014, up from 158 GW at the end of 2008, with an average annual growth rate of 20.9% [2]. Horizontal wind turbines are the least expensive and clean way to harness this important energy source. However, for the design and development of more efficient and reliable wind turbines, accurate prediction of aerodynamic behavior is of critical significance, since the interaction of the wind with the blades influences the efficiency. It also has a significant effect on the loads on bearings and gearbox, ultimately affecting the lifespan and reliability of the machine.

The flow in wind turbines, even in very large ones, is still essentially incompressible, with Mach numbers based on blade tip speed rarely exceeding 0.25. This fact justifies the use of incompressible fluid solvers for most wind turbines. Methods of various levels of complexity to predict the aerodynamic behavior of a wind turbine rotor have been developed. Being computationally cheap and highly efficient, blade element momentum methods (BEM) have been very popular for engineering design, provided that good airfoil data are available for lift and drag coefficients as a function of angle of attack [3]. Several codes and models were developed based on BEM and their performance was improved by introducing new correction models such as tip loss and dynamic stall corrections [4,5]. However, BEM models are greatly influenced by the choice of airfoil data and dependent on empirical corrections to two-dimensional (2D) airfoil results to account for three-dimensional (3D) effects, such as tip loss, rotational flow, and dynamic stall [6]. To obtain more physics of wind turbine aerodynamics and retain high computational efficiency, 3D inviscid aerodynamic models, in which viscous effects are neglected, were introduced, including lifting line [7], panel [8], vortex [9], and Boundary Integral Equation (BIEM) [10] methods. Nevertheless, issues arise because potential flow methods cannot handle viscous effects and separation. The next level of complexity is to solve the Reynolds-Averaged Navier–Stokes (RANS) equations with some turbulence models, or the more advanced and costly Detached Eddy Simulation (DES) approaches that combine the accuracy of large eddy simulation (LES) inside the separation region for vortical structures and

* Corresponding author. Tel.: +1 319 335 6381; fax: +1 319 335 5238.
E-mail addresses: yuwei-li@uiowa.edu (Y. Li), kwangpaik.paik@samsung.com (K.-J. Paik), xingtao@gmail.com (T. Xing), pablo-carrica@uiowa.edu (P.M. Carrica).
[1] Tel.: +1 319 855 3279; fax: +1 319 335 5238.
[2] Present address: Samsung Heavy Industries, Daejeon, South Korea.
[3] Tel.: +1 208 885 6579 (office); fax: +1 208 885 9031.

0960-1481/$ – see front matter © 2011 Elsevier Ltd. All rights reserved.
doi:10.1016/j.renene.2011.06.029

efficiency of RANS inside a boundary layer. This gives DES the ability to better resolve flow separation and the stall of the airfoil [11]. Though the cost of these approaches is significantly higher than any of the previously mentioned simpler methods, advances in computer technology make it possible to handle large, dynamic problems with parallel platforms.

Most computations to date testing numerical methods are compared to the National Renewable Energy Laboratory (NREL) Unsteady Aerodynamics Experiment (UAE) [12,13], which provides comprehensive high-quality data for a modified Grumman 20 kW twin-bladed turbine, tested in the wind tunnel at NASA Ames. The most important results are in the Phase VI of the experiments. A blind numerical study involving 20 different participants using various CFD codes was conducted subsequently [14].

Several authors have performed CFD computations of wind turbines with a variety of methods. Sezer-Uzol and Long [15] computed the NREL Phase VI turbine at different wind speeds and yaw angles using the finite volume flow solver PUMA2 with rotating unstructured tetrahedral grids, showing good agreement with experiment, but the inviscid nature of the code resulted in limited ability to predict situations when massive flow separation occurs. Sørensen et al. [16] studied 3-D aerodynamic effects as a function of wind speeds by using the multiblock finite volume, incompressible RANS flow solver EllipSys3D with a rotor-only configuration. Good qualitative and quantitative agreement with experimental measurements evidenced the advantages of CFD approaches for wind turbine simulation. Perhaps the most comprehensive aerodynamic study to date has been performed by Duque et al. [17], who performed computations of the NREL Phase VI turbine with the NASA compressible RANS flow solver Overflow-D, based on a finite differences approach and overset grid [18]. The authors compare the results of Overflow-D and the lifting line code CAMRAD II with the experiments, and extensively discuss the aerodynamic performance of the wind turbine, including shaft power, normal force and pressure coefficient. Potsdam and Mavriplis [19] used the unstructured multigrid RANS code NSU3D to predict the aerodynamics of an isolated wind turbine rotor, and the results were compared with both the experiments and the predictions with the code Overflow. Bazilevs et al. [20] studied the rotor of the NREL 5 MW baseline wind turbine [21] using both a finite element approach and a NURB-based (Non-Uniform Rational B-splines) approach for the geometry, which has the potential for coupled aerodynamic/structural analysis.

Notice that most studies consider the rotor-only geometry, excluding the tower and nacelle; in most cases only one blade was included in the simulation. These simplifications are understandable because the resulting grid is static throughout the calculation and thus greatly alleviate the computational complexity and cost, but they can leave out some important effects. Dynamic moving overset grids is one of the methods that allow for computation of bodies with relative motions, including elastic deformation.

The objective of this paper is to present transient computations of the full-scale NREL Phase VI turbine. The study is performed using the incompressible, dynamic overset code CFDShip-Iowa v4.5 with a hierarchy of objects that include the blades, rotor, nacelle, and tower/ground, allowing variations of blade pitch angle and yaw during the computations. The tests include cases with a fixed blade pitch angle (3°) and variable wind speeds, and variable pitch angles at fixed wind speed (15 m/s). All tests are performed at a constant rotational speed of 72 RPM. For these cases extensive comparison with experimental data is performed and the results are analyzed.

2. Mathematical and numerical methods

The general purpose code CFDShip-Iowa v4.5 is used to perform the wind turbine computations. CFDShip-Iowa v4.5 is a finite difference, general-purpose unsteady Reynolds-Averaged Navier-Stokes (URANS) or Detached Eddy Simulation (DES) overset solver. The air side is treated with a semi-coupled approach, in which the water ignores the presence of the air but the air is computed using the water free surface as an immerse boundary, thus providing an excellent approximation to the air flow and forces on large-scale objects like ships or floating structures [22]. The free surface is modeled with a level set approach, enforcing kinematic and dynamic free surface boundary conditions on the interface [23]. Dynamic overset grids are used to resolve grid deformation and relative motions [24], where the overset connectivity is provided at run time by the code Suggar [25], which allows dynamic interpolations. The code and the overset strategy have recently been optimized for large-scale computations [26]. The code has capabilities for full six degree of freedom (6DOF) and a parent/child hierarchy of objects that allows motion of control surfaces and other appendages. Autopilots based on proportional-integral-derivative (PID) controllers allow control of heading, speed or attitude. Fluid-structure interaction (FSI) can also be modeled by using either modal superposition for linear problems or a structure solver based on finite element method for non-linear problems [27]. Convection terms are discretized with finite differences second-order upwind (for RANS) or fourth-order upwind biased (for DES or delayed DES), and with a second-order centered scheme for the viscous terms. The temporal terms are discretized using a second-order backwards Euler scheme. Incompressibility is enforced by a strong pressure/velocity coupling, achieved using either the pressure implicit with splitting of operators (PISO) or projection algorithms.

Specific discussion follows on terms related to the computation of the wind turbine. For complete details on the mathematical and numerical methods the reader is referred to the cited references and the literature therein.

2.1. Governing equations

Mass and momentum conservation equations are written in dimensionless form as follows:

$$\nabla \cdot \boldsymbol{u} = 0 \tag{1}$$

$$\frac{\partial u}{\partial t} + \boldsymbol{u} \cdot \nabla \boldsymbol{u} = -\nabla p + \nabla \cdot \left[\frac{1}{\mathrm{Re}_{\mathrm{eff}}} \left(\nabla \mathbf{u} + \nabla \mathbf{u}^T \right) \right] + \mathbf{S} \tag{2}$$

where $\mathbf{u}$ is the fluid velocity and $\mathbf{S}$ is a source term, zero in this paper. p is the non-dimensional pressure, $\mathrm{Re}_{\mathrm{eff}}$ is the effective Reynolds number, defined as:

$$p = \frac{p_{\mathrm{abs}}}{\rho U_0^2} + \frac{2}{3} k \tag{3}$$

$$\mathrm{Re}_{\mathrm{eff}} = \frac{U_0 L}{\nu + \nu_t} \tag{4}$$

where p_{abs} is the absolute pressure, U_0 and L are the free-stream velocity and characteristic length (in this case the radius of the blade) respectively, ν_t is the turbulent eddy viscosity, and k is the turbulent kinetic energy.

2.2. Turbulence modeling

The turbulence is modeled using a blended $k-\omega/k-\varepsilon$ shear stress transport (SST) model [28], in which the turbulent kinetic energy k and specific dissipation rate ω are

$$\frac{\partial k}{\partial t} + (\mathbf{u} - \sigma_k \nabla \upsilon_t) \cdot \nabla k - \frac{1}{P_k}\nabla^2 k + s_k = 0 \tag{5}$$

$$\frac{\partial \omega}{\partial t} + (\mathbf{u} - \sigma_\omega \nabla \upsilon_t) \cdot \nabla \omega - \frac{1}{P_\omega}\nabla^2 \omega + s_\omega = 0 \tag{6}$$

where the turbulent viscosity and effective Peclet numbers are defined as

$$\upsilon_t = \frac{k}{\omega}, P_k = \frac{1}{\frac{1}{\mathrm{Re}} + \sigma_k \upsilon_t}, P_\omega = \frac{1}{\frac{1}{\mathrm{Re}} + \sigma_\omega \upsilon_t} \tag{7}$$

and the source terms for k and ω are

$$s_k = -G + \frac{k^{3/2}}{l_{k-\omega}} \tag{8}$$

$$s_\omega = -\gamma \frac{\omega}{k} G + \beta^* \omega^2 - 2(1 - F_1)\, \sigma_{\omega 2} \frac{1}{\omega} \nabla k \cdot \nabla \omega \tag{9}$$

where the length scale is $l_{k-\omega} = \sqrt{k}/(\beta^* \omega)$ and the kinetic energy production is $G = \upsilon_t \tau : \nabla \mathbf{u}$. The blending function that switches between the $k-\omega$ model near the wall to the $k-\varepsilon$ model on the free stream region is

$$F_1 = \tanh\left[\left(\min\left(\max\left(\frac{\sqrt{k}}{0.09\omega\delta}; \frac{1}{\mathrm{Re}}\frac{500}{\delta^2 \omega}\right); \frac{4\sigma_{\omega 2} k}{CD_{k\omega}\delta^2}\right)\right)^4\right] \tag{10}$$

where δ is the distance to the nearest no slip surface and $CD_{k\omega} = \max(2\sigma_{\omega 2}\frac{1}{\omega}\nabla k \cdot \nabla \omega; 10^{-20})$. This model takes advantage of the benefits of the $k-\omega$ model, e.g. does not require near-wall damping function and uses simple Dirichlet boundary conditions at solid walls, and of the $k-\varepsilon$, e.g. less sensitive to the level of free-stream turbulence.

DES modeling follows Travin et al [29], where the length scale is computed as

$$\tilde{l} = \min(l_{k-\omega}, C_{DES}\Delta) \tag{11}$$

where Δ is the grid length scale, taken as the maximum cell length side, and

$$C_{DES} = (1 - F_1)C_{DES}^{k-\varepsilon} + (1 - F_1)C_{DES}^{k-\omega} \tag{12}$$

with $C_{DES}^{k-\varepsilon} = 0.61$ and $C_{DES}^{k-\omega} = 0.78$. Delayed-DES (DDES) modeling in CFDShip-Iowa follows the approach of Sainte-Rose et al. [30].

For the simulations presented in this paper, integration all the way to the wall is used (no wall functions). The SST model then requires wall refinement to satisfy $y^+ \leq 1$.

3. NREL phase VI turbine and grid strategy

The testing wind turbine is the NREL phase VI, a modified Grumman Windstream 33 stall-regulated turbine with full-span pitch control and a power rating of 20 kW. It has 2 blades, with NREL s809 tapered and twisted blade profile. The rotor diameter is 10.058 m while hub height is 12.192 m. The experiments were performed in the NASA Ames wind tunnel in 1999 and are considered a benchmark for evaluation of wind turbine aerodynamics computer codes. Detailed geometry, machine parameters and experimental procedures can be found in the NREL report [12].

Two cases were selected from the test matrix of the NREL experiments, belonging to sequences S and K. In particular, simulations for sequence S are used to evaluate the ability of the code to predict the aerodynamics under different wind velocities (5, 10, 15 and 25 m/s) at a fixed 3° blade tip pitch angle. Simulations for sequence K are designed to evaluate the performance of the 3D blade in the presence of rotation to different static angles of attack by varying the blade tip pitch angles from 40° to −15° in steps of 5°. The wind velocity for sequence K is fixed at 15 m/s (the experimental data also evaluates 6, 10 and 20 m/s). For both cases the rotational speed is 72 RPM. Several yaw angles were tested experimentally, but only those with the yaw angle fixed at 0° were simulated. Table 1 summarizes all CFD simulation cases.

RANS and DES computations were conducted for sequence S to investigate the response of the two methodologies for wind turbine modeling, while only DES was applied to sequence K. In both cases hybrid 2^{nd}–4^{th} order schemes were used for convection.

The grid design for sequences S and K is shown in Fig. 1. The geometries of the nacelle and hub have been approximated and do not correspond to the true shape of the NREL phase VI turbine. The grid system consists of 13 overset blocks to discretize the blades, hub, nacelle, tower and floor. The blades themselves are each gridded with an O-type block to cover the span, one block for the tip and one for the root. O blocks are used for the hub and nacelle as well as for the tower. A refinement block is used to match the nacelle grid with those from the hub/blade roots/tower systems. Finer refinements are used to capture the flow around the rotor using a Cartesian block and an O-type block. Overall 52.3 million grid points are used, distributed in 2048 domains each sent to a processor, with an average of 28 046 grid points per processor and a maximum deviation around the average of 2.2% maximum. After splitting, the 52.3 million grid points increase to 57.4 million due to duplication on the block to block interfaces, see Table 2.

Since surface overset grids are used, the computation of forces and areas requires evaluation of the portions that are overset to avoid double-counting in overlaid areas. This is done as a pre-processing step with the code Usurp [31], which generates weights that alter the area of each cell on the solid body to provide the appropriate forces and areas at each cell.

The grids are organized in a parent/child hierarchy, as shown in Table 2. The grids comprising the blades can pitch about the pitching axis, while these and the hub form the rotor, which rotates about the shaft axis. The nacelle and the rotor form the body Nacelle which can rotate about the tower axis with the yaw angle. In this way a fully controlled turbine can be simulated, with a rotational speed controller acting on the blade pitch and an attitude controller acting on the yaw. In this work the yaw is kept at 0°, but the pitch is modified dynamically to perform the simulations of sequence K. The time step was chosen such that the blades rotate 1° per time step for cases with 5–15 m/s wind speed, and 0.5° for cases with 25 m/s wind speed.

4. Results and discussion

4.1. Variable wind speed at constant pitch angle

The experimental sequence S comprises data at 3°of blade pitch for wind speeds from 5 to 25 m/s at intervals of 1 m/s. The CFD study is focused on 5, 10, 15 and 25 m/s. The highest two wind speeds correspond to stall conditions in most of the blade and simulations are thus challenging. This is shown in Fig. 2, which illustrates the vortical structures using iso-surfaces of the second invariant of the rate of strain tensor [32] at $Q = 5$. It is clear that these DES computations predict fully attached flow for 5 and 10 m/s, with development of unsteady trailing vortices at 10 m/s. At these two velocities the blade tip vortices are strong and stable. Strong vortices detach also from the tower and the roots of the blades, where the geometry changes quickly from the s809 profile to cylindrical posts attached to the hub. Notice that the vortical

Table 1
Simulation cases.

Case no.	Nominal wind speed [m/s]	Re (based on blade length)	Pitch [degree]	Run	RANS/DES
1	5	1.766×10^6	3	S0500000	RANS
2	15	5.205×10^6	3	S1500000	RANS
3	25	8.645×10^6	3	S2500001	RANS
4	5	1.766×10^6	3	S0500000	DES
5	10	3.535×10^6	3	S1000000	DES
6	15	5.205×10^6	3	S1500000	DES
7	25	8.645×10^6	3	S2500001	DES
8	15	5.241×10^6	−15 to 40 in 5 degree steps	K1500ST1	DES

structures dissipate quickly away from the regions covered by grid refinements, downstream of the rotor plane and at the tower below 1 blade length. At 15 m/s about the outer half of the blade experiences massive unsteady separation, while at 25 m/s most of the blade suffers massive unsteady flow separation. For these two higher velocities the interaction of the tip vortices with the unsteady separation from the suction side of the blades causes breakdown of the tip vortices, very dramatically at 25 m/s. Electronic Annexes I, II, III and IV show animations of the vortical structures colored with axial speed obtained with DES for wind speeds of 5, 10, 15 and 25 m/s, respectively, in a blade-fixed reference frame. The unsteadiness and regions of attached or separated flow on the blades under different conditions are clear in these animations. Animations of DES simulations at 5 and 25 m/s on the earth reference frame are shown in Electronic Annexes V and VI, respectively. The animations show the separation on the tower and nacelle in a more transparent way. Note how the tower vertical vortices tend to evolve into hairpin vortices and into smaller structures as the wind speed increases. The formation of these hairpin vortices is interesting, since it requires the presence of gradients of streamwise velocities [33], which in this case occur along the rotor, and especially by the rotor tip vortex.

Supplementary video related to this article can be found at doi: 10.1016/j.renene.2011.06.029

Fig. 3 shows comparisons of predicted vortical structures at two wind speeds for RANS and DES computations. At 5 m/s both methods predict essentially the same flow around the blades. More vortices can be observed for DES in the separated flow regions close to the hub, tower and nacelle, but these have lesser effect on the performance of the turbine. At wind speed of 25 m/s the differences between RANS and DES are more dramatic. In particular the separation bubbles on the suction side of the blade are highly unsteady and are shed periodically for the DES computation, while they are mostly steady for RANS. This causes a stable tip vortex for RANS, while the tip vortex breaks down for DES, as previously discussed. Animations of RANS simulations in the earth reference frame are shown in Electronic Annexes VII and VIII for 5 and 25 m/s, respectively. Notice in Electronic Annexes IV and VIII that the separation bubble is essentially steady in RANS but highly unsteady with DES.

The experimental thrust and torque (and thus power) are obtained integrating the pressure measurements along the blade, and consequently the friction effects are neglected. CFD computations account for both pressure and friction forces. Figs. 4 and 5 show comparisons of thrust and power between DES-based CFD and NREL experiments for Sequence S. In all figures the vertical bars represent the experimental standard deviation, not the error or experimental uncertainty, which is not reported in [13]. Overall CFD simulations predict very well the general performance of the turbine, even at the two highest wind speeds where stalled flows occur. CFD predictions of the thrust are all well within the standard

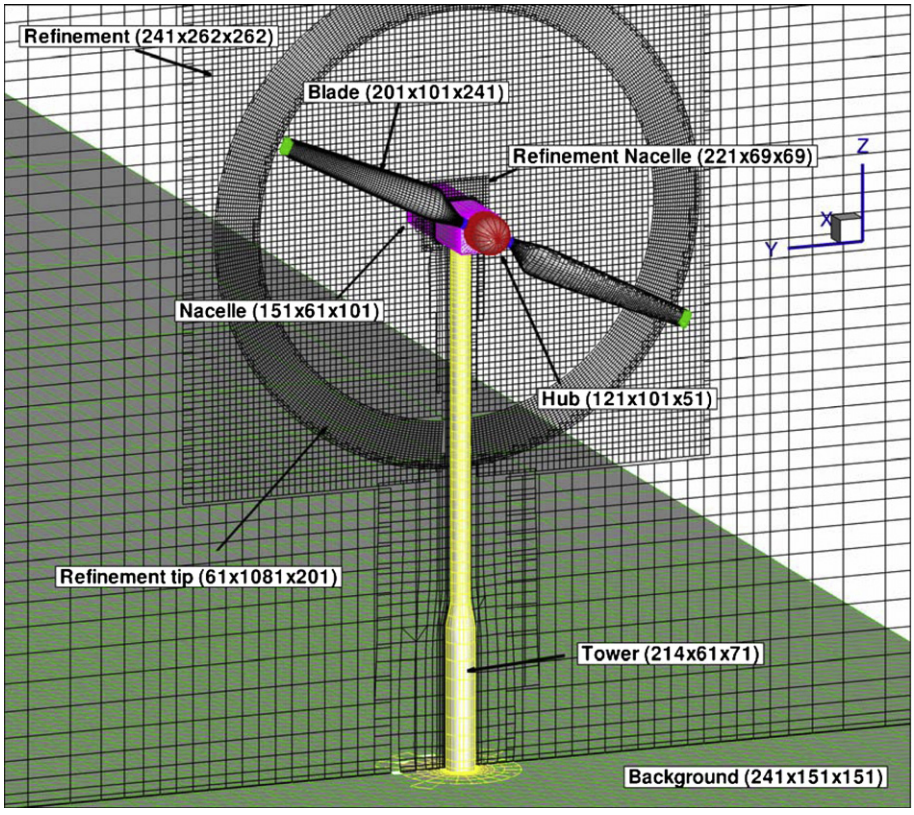

Fig. 1. Grid design. Grid points are skipped in all directions for clarity.

Table 2
Grid details.

Name	imax	jmax	kmax	Procs	isplit	jsplit	ksplit	Processor points	Total	Hierarchy
Hub	121	101	51	24	41	26	26	27716	665K	Rotor-Nacelle
Blade 1	201	101	241	192	35	26	31	28210	5.41M	Blade-Rotor-Nacelle
Tip 1	121	101	101	48	41	26	26	27716	1.33M	Blade-Rotor-Nacelle
Root 1	201	101	31	24	35	26	31	28210	677K	Blade-Rotor-Nacelle
Blade 2	201	101	241	192	35	26	31	28210	5.41M	Blade-Rotor-Nacelle
Tip 2	121	101	101	48	41	26	26	27716	1.33M	Blade-Rotor-Nacelle
Root 2	201	101	31	24	35	26	31	28210	677K	Blade-Rotor-Nacelle
Refinement	241	262	262	648	31	30	30	27900	18.08M	Earth
Ref. Tip	61	1081	201	512	31	35	26	28210	14.44M	Nacelle
Ref. Nacelle	221	69	69	40	23	35	35	28175	1.13M	Nacelle
Tower	214	61	71	36	37	31	25	28675	1.03M	Earth
Nacelle	151	61	101	36	26	31	35	28210	1.02M	Nacelle
Background	241	151	151	224	31	39	23	27807	6.23M	Earth
Total				2048				Ave: 28046	57.43M	

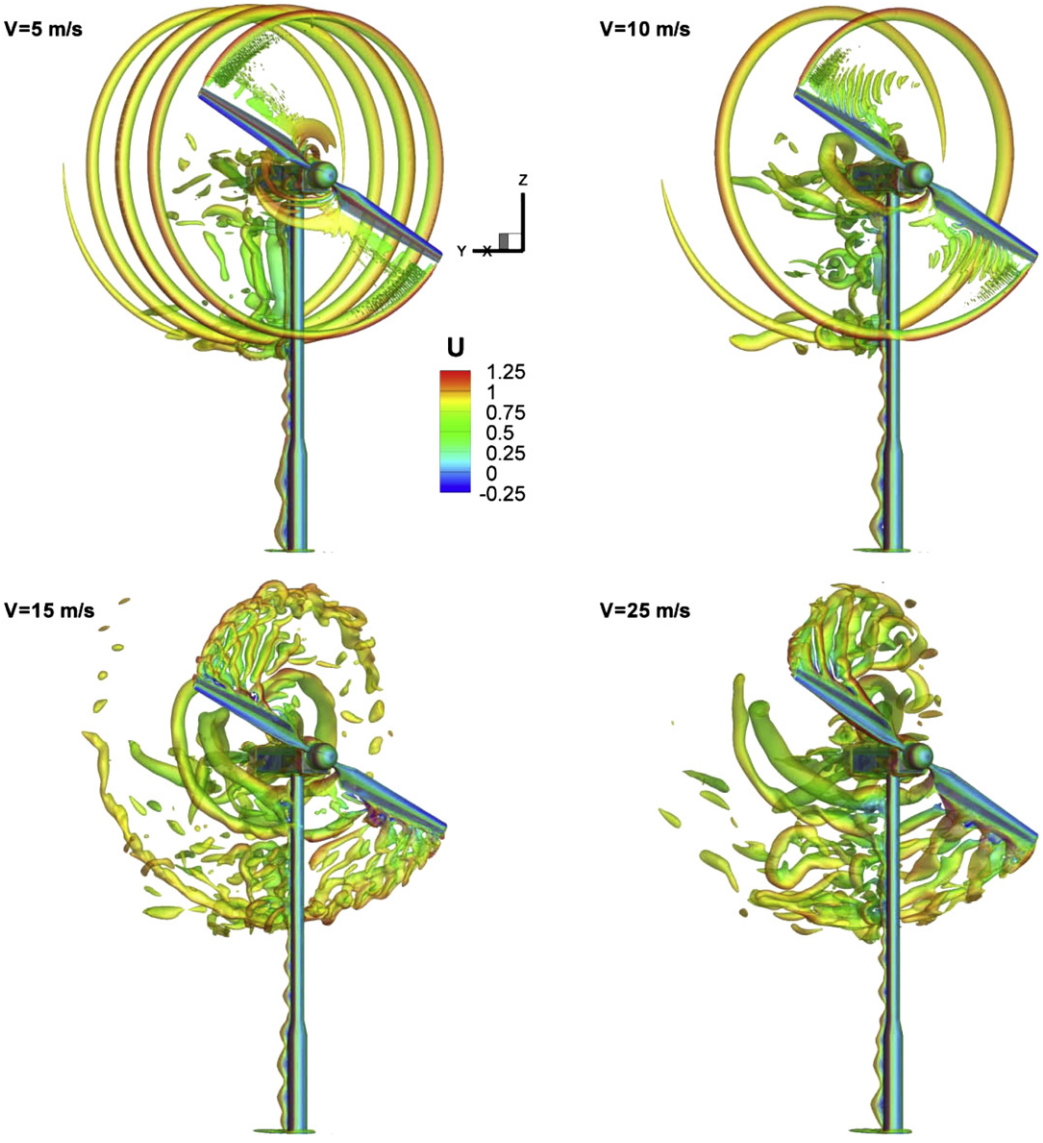

Fig. 2. Vortical structures represented by iso-surfaces of $Q = 5$ for different velocities (pitch angle 3°).

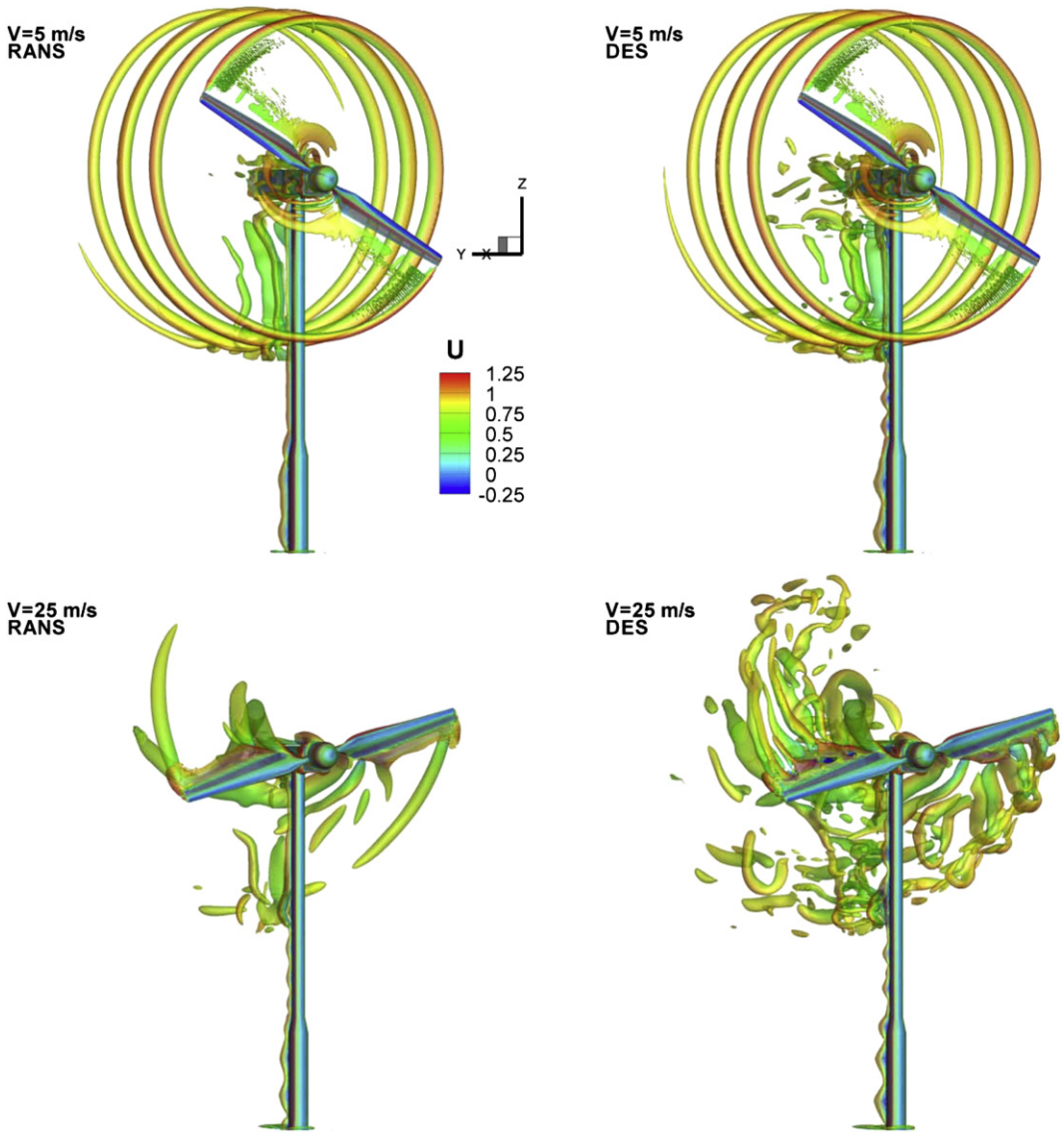

Fig. 3. Comparison of vortical structures predicted by RANS and DES for low (5 m/s) and high (25 m/s) wind speeds. Vortical structures are represented by iso-surfaces of $Q = 5$ (pitch angle 3°).

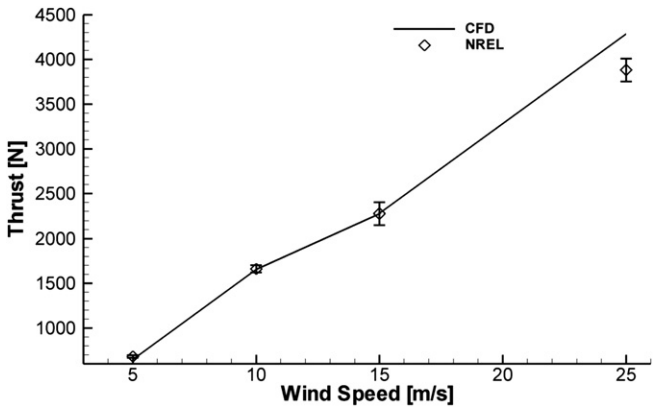

Fig. 4. Thrust for different velocities (pitch angle 3°).

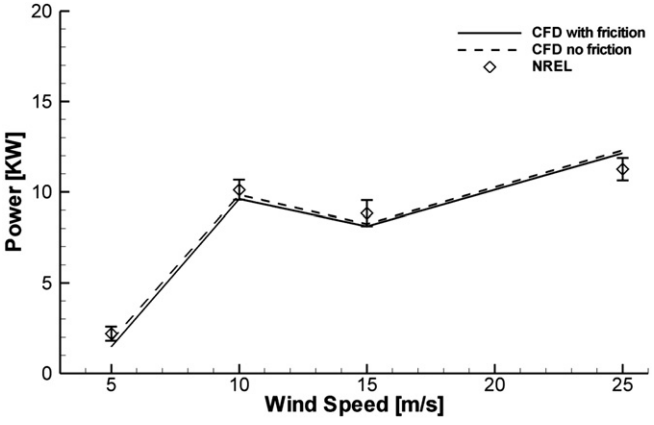

Fig. 5. Power to the shaft for different velocities (pitch angle 3°).

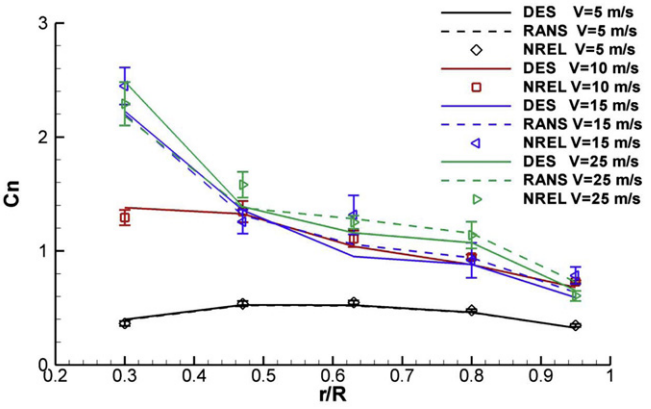

Fig. 6. Normal force coefficients for different velocities at 5 radial sections (pitch angle 3°).

deviation of the experimental measurements, except for a slight over prediction at 25 m/s where as previously shown stalled flow and separation are pronounced. The friction component on the total thrust is negligible. Power is a bit underpredicted, except for the highest speed. In addition, results neglecting friction in the computation of the forces are closer to the experimental data as expected, but the friction force contribution is still small except at slower wind speeds. Notice that the code predicts properly the flattening of the power as a function of the wind speed as the turbine becomes stall-controlled at higher wind speeds.

As thrust and power are parameters integrated over the area of the blades, evaluation of sectional force coefficients such as radial normal force coefficient C_n allows a better check on the ability of the code to properly capture the aerodynamic behavior of the wind turbine. The normal force coefficient is still an integration of pressure but limited to a section of the blade. As pointed out by Simms et al. [34], who summarized blind predictions of several codes for the Phase VI turbine, good prediction of integrated parameters can be obtained with models that over predict aerodynamic forces on the inboard part of the blade, while under predicting the forces outboard. Fig. 6 compares RANS and DES CFD and experimental results of C_n at 5 different sections of the blade. Both RANS and DES match very well the experimental measurements for all wind velocities simulated. In particular, at lower wind velocities (5 m/s) where no flow separation occurs except at the transition section near the root, RANS and DES simulations show accurate predictions with little difference between each other, as expected from the similarity shown in the flow regimes from Fig. 3. At higher wind velocities, where flow separation becomes more important and vortex shedding occurs, discrepancies appear gradually. At 15 m/s RANS and DES results are very similar for $r/R < 0.5$ where the flow around the blade separates weakly (see Fig. 2 and

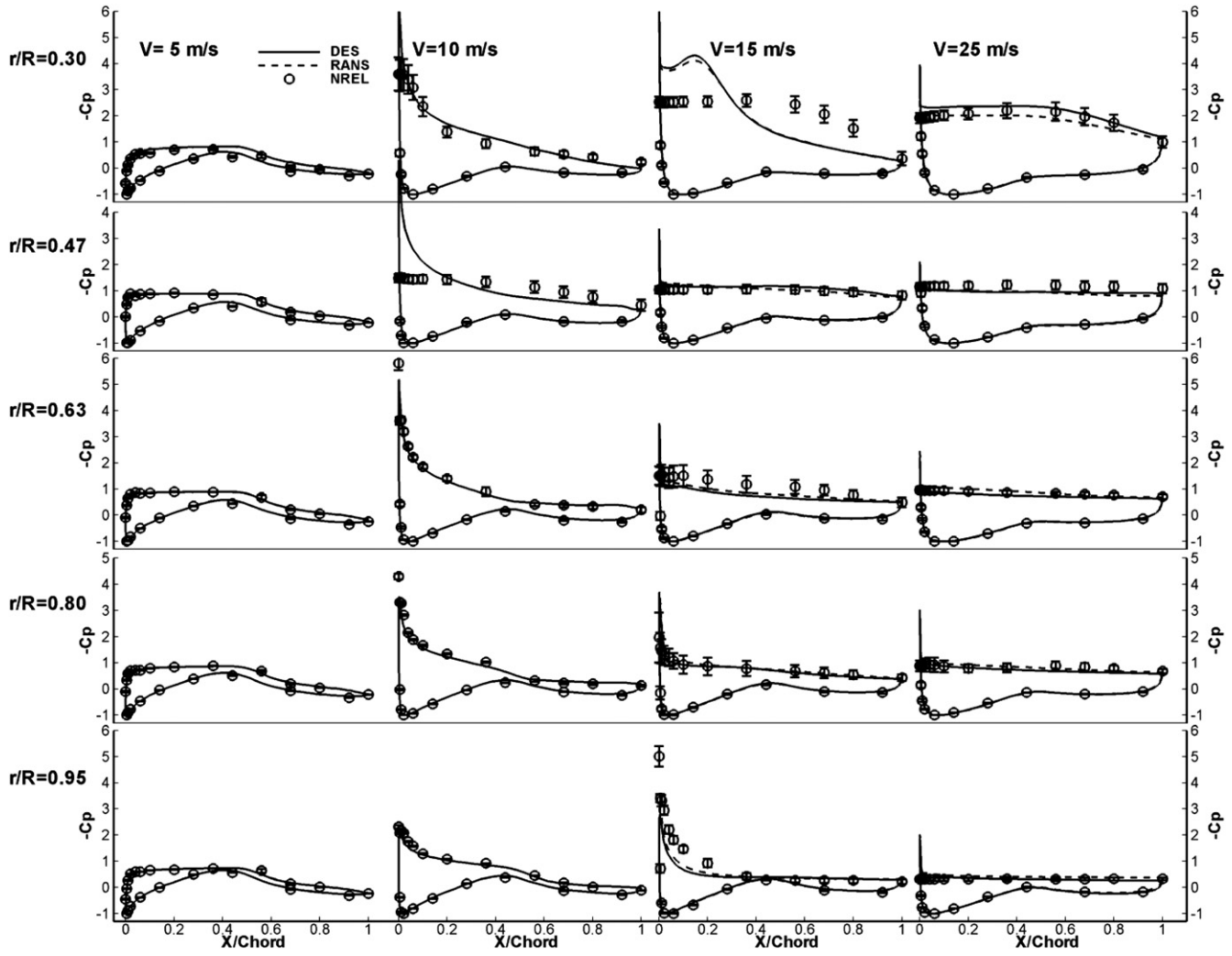

Fig. 7. Pressure coefficient for different velocities on 5 blade sections (pitch angle 3°).

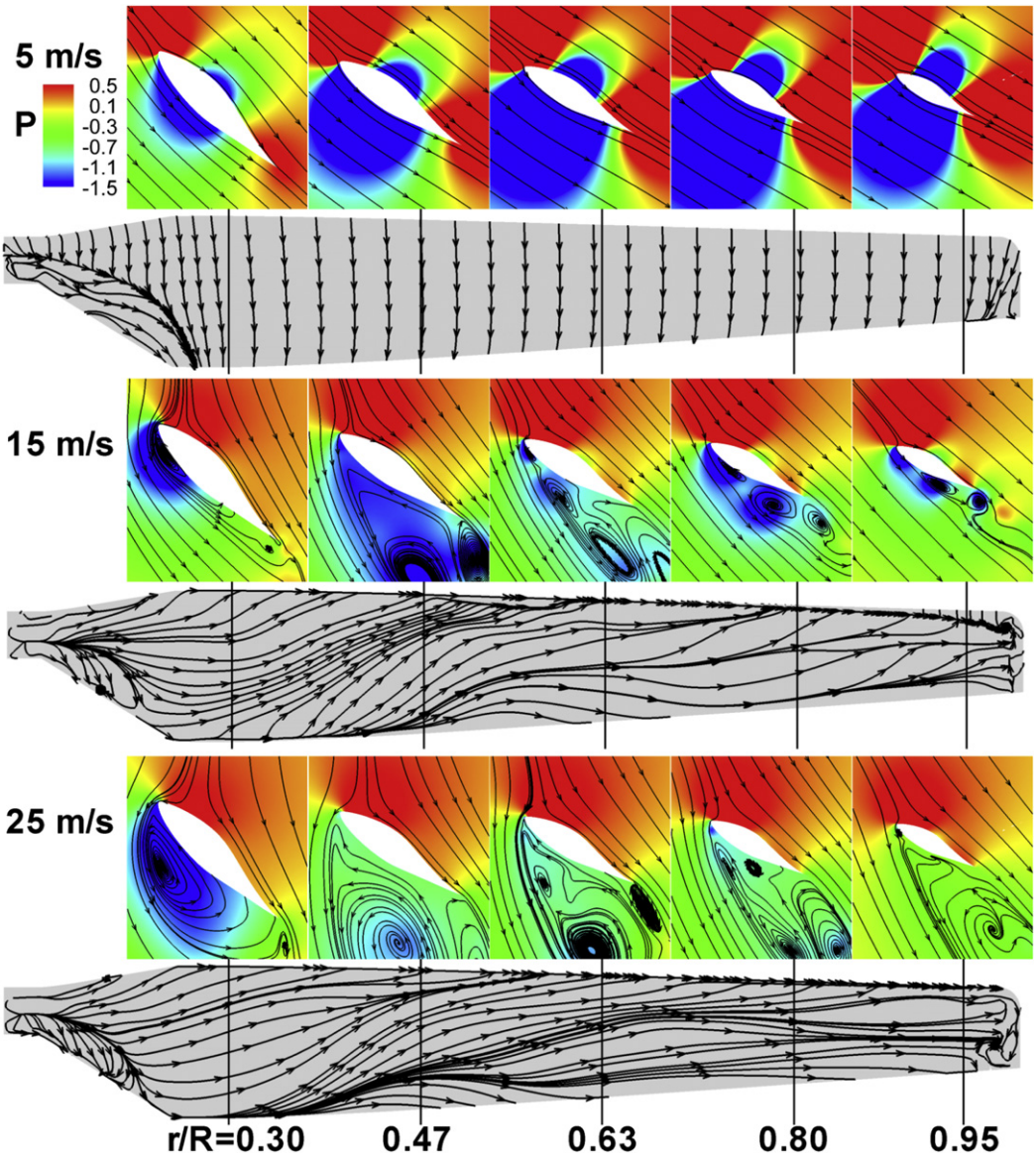

Fig. 8. Limiting streamlines on the suction side of the blade and selected sections (colored with pressure) for 3° pitch angle.

Electronic Annex III for the DES results), but differ more for $r/R > 0.5$ where separation and vortex shedding are important and differences in flow pattern between RANS and DES are remarkable. At 25 m/s the differences between RANS and DES are significant for all sections, as expected from the dramatic difference in flow patterns shown in Fig. 3. Observe that RANS computations tend to predict more lift as the flow remains attached at larger angles of attack. All normal force coefficients are well predicted with DES with the exception of section $r/R = 0.63$ at $V = 15$ m/s and section $r/R = 0.47$ at $V = 25$ m/s. Large differences in normal force coefficients at these sections and wind speeds are also shown in the computations of Duque et al. [17].

Direct comparisons of the pressure coefficient C_P between CFD and experimental data at 5 different sections as a function of wind speed are shown in Fig. 7. The pressure coefficient is a harder test for CFD since it is a local quantity, and comparison is made against pressure taps installed in the blade. See that the incompressible formulation of CFDShip-Iowa, appropriate for wind turbines, does not produce the spurious pressure peaks observed on compressible codes [17]. At low wind speeds the CFD predictions match the experimental data remarkably well. For 10 m/s at $r/R = 0.47$ the experiments show a flat pressure on the suction side, indicating separation, while CFD results predict a leading edge peak. The same behavior occurs for 15 m/s at $r/R = 0.30$, where CFD predicts a peak at 0.2 chord lengths downstream of the leading edge while experimental results show a more flat pressure distribution. Notice that the integral of the pressure for these two anomalous conditions will be about the same for CFD and experiments, resulting in good prediction of the normal force coefficient. Duque et al. [17] argued that possibly unsteadiness is the reason for these discrepancies, since they used the code Overflow-D in steady-state mode. This is not supported by the current simulations as similar differences are observed for DES that captures significant unsteadiness in the trailing edge on the suction side both for 10 m/s at $r/R = 0.47$ and for 15 m/s at $r/R = 0.30$ (see Electronic Annexes II and III). It is possible that CFD grossly under-predicts the separation, though it is hard to think of a mechanism that would separate locally at $r/R = 0.47$ for $V = 10$ m/s while all other sections inboard and outboard are attached. The two points in Fig. 6 that show the largest errors, section $r/R = 0.63$ at $V = 15$ m/s and section $r/R = 0.47$ at

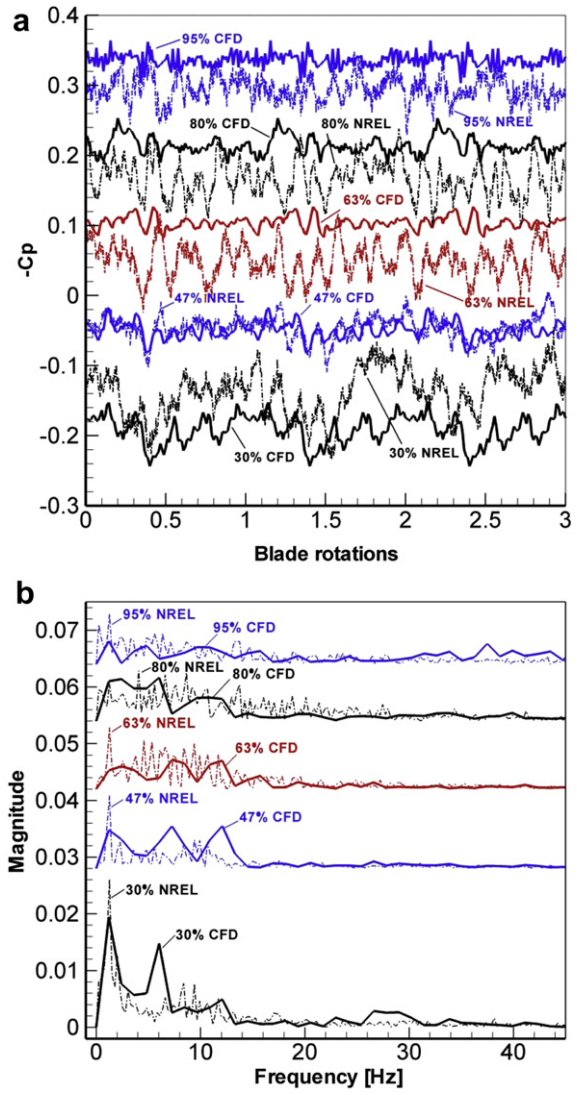

Fig. 9. Cp on five sections for 15 m/s, 3° pitch: (a) time histories, (b) FFT.

V = 25 m/s, show significant under prediction of the suction pressure and thus result in lower integral inside the curves.

Fig. 8 shows instantaneous limiting streamlines on the blade, along with streamlines on the projected velocities at the selected sections. At low wind speed (5 m/s) the CFD computations predict fully attached flow everywhere in the active blade, and some separation where the s809 blade profile merges to a cylindrical section. At this speed the pressure stays low on the suction side and the blade provides consistent lift. At 15 m/s the flow exhibits significant separation at all sections, with smaller scale, unsteady vortices shed in the second half of the blade (see also Electronic Annex III). For section r/R = 0.47 at this speed the flow separates from the leading edge and reattaches to the blade surface to form a closed separation bubble whereas all other sections show open separation where vortices are shedding away from the blade surface to the wake. Significant pressure recovery is observed, mostly for the outer sections. Similar trends are observed for all sections at 25 m/s, but the separation is stronger with violent vortex shedding, with very little pressure recovery on the suction side indicating massive stall (see also Electronic Annex IV).

Time histories of Cp for 15 m/s at 3° blade pitch angle are shown in Fig. 9a, and the corresponding frequency spectra are shown in Fig. 9b. The time evolution is expressed in terms of blade rotations with the blade down at zero rotations. The measurements were taken at five different points on sections r/R = 0.30, 0.47, 0.63, 0.80 and 0.95 at 44% of the chord from the leading edge on the pressure side. The CFD values correspond to one rotation saving every 4 (5–15 m/s) or 8 (25 m/s) time steps (90 points per rotation) and are repeated three times, due to the cost of saving large number of volume solutions and the corresponding processing. Because the absolute pressures are small, the differences between the mean values for experiments and CFD appear large for all sections except r/R = 0.47, but the largest error occurs at r/R = 0.30 and is less than 2.5% of the pressure dynamic range at that section, see Fig. 7.

Notice in Fig. 9b that the amplitude of the fluctuations is in general larger in the experiments than in CFD. At r/R = 0.30 the presence of the tower is clear, shown in Fig. 9a as an increase in pressure at integer rotations (0, 1, 2, etc.), and in Fig. 9b as a peak at 1.2 Hz, the rotational frequency. Large amplitudes at 1.2 Hz and 2.4 Hz are present at all sections, but the amplitude decreases for larger radii. Most of the frequency content is limited to frequencies below 10 Hz, as can be expected for a machine of this size. In CFD these high frequencies can be associated with vortex shedding (see Electronic Annex III to observe the phenomena). The magnitude of the fluctuations is larger in the experiments than in CFD at the other sections, but the difference is more evident at r/R = 0.63.

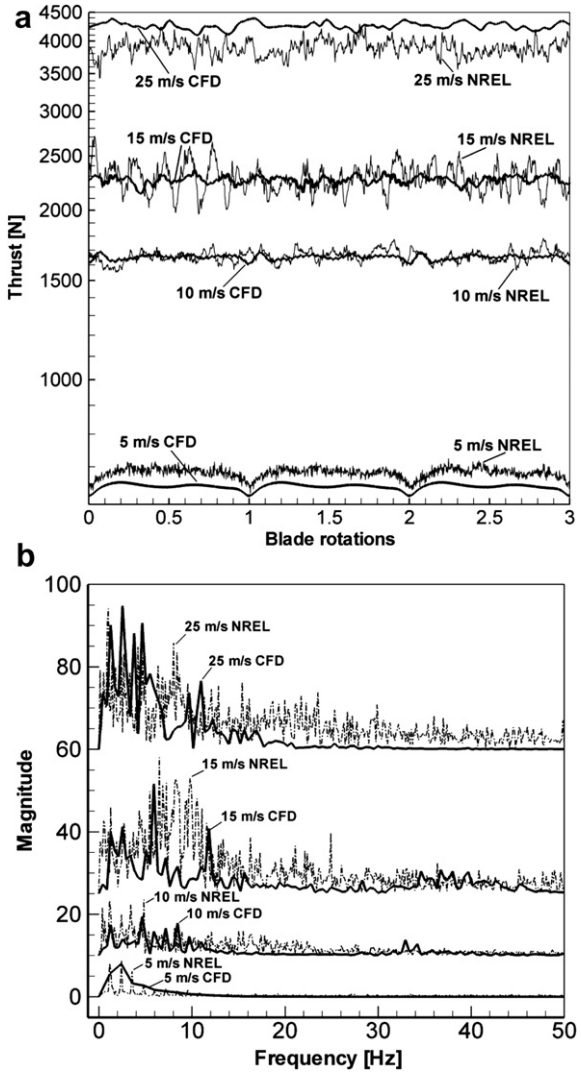

Fig. 10. Thrust for different velocities, 3° pitch: (a) time history, (b) FFT.

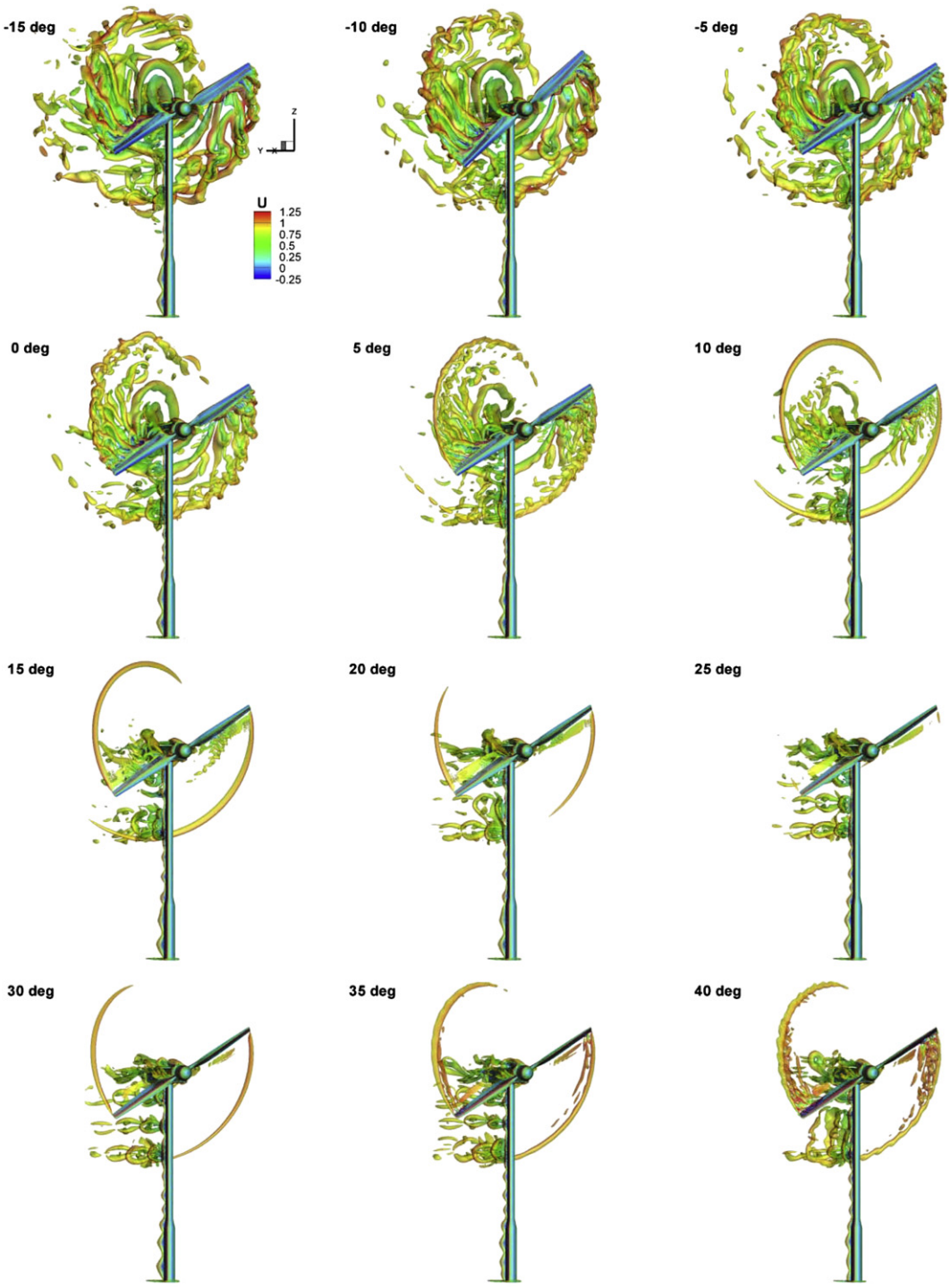

Fig. 11. Vortical structures represented by iso-surfaces of $Q = 5$ for different pitch angles (wind velocity 15 m/s).

Notice that the frequency content in CFD is comparable with the experiments, indicating that the turbulence model is able to capture most of the oscillations caused by organized vortical structures and fluctuations caused by turbulent structures. On the same line of analysis, the turbulence model seems to fail to capture the amplitude of the pressure fluctuations, likely due to insufficient grid discretization to maintain the low pressure on the vortex cores, though other causes may be speculated that would cause differences in pressure fluctuation amplitudes, like blade vibrations caused by gears and bearings and by the elasticity of the blade. All these effects are neglected in CFD.

Time histories of thrust for 5, 10, 15 and 25 m/s at 3° blade pitch angle are shown in Fig. 10a, and the frequency spectra in Fig. 10b. In this case the forces are saved every time step, so there are 1080 points in CFD for 5–15 m/s and 2160 for 25 m/s. To compare with the experiments fairly, the thrust in one blade is multiplied by two instead of using the thrust in both blades, which would smooth the transient behavior of CFD by adding two blades that have different instantaneous forces. The experimental thrust was obtained by integrating the pressures measured on the five sections at $r/R = 0.30$, 0.47, 0.63, 0.80 and 0.95, while CFD forces are integrated on every grid cell on the blade, smoothing transients more than in

the experimental evaluation of the force by averaging local pressure highs with local pressure lows. It is not surprising then that the experiments show larger fluctuation amplitudes than CFD, though a significant portion of the larger fluctuations is likely due to inadequacy of the turbulence model to fully capture the transient instabilities observed in the flow, as discussed in the previous paragraph. Fig. 10a clearly displays a decrease in thrust when the blade is in the downward position, indicating that the presence of the tower has a small but appreciable effect. This effect is most marked at 5 m/s and decreases with speed to be completely masked by fluctuations at 25 m/s. Perceive that at 5 m/s CFD shows no fluctuations since the flow does not separate (see also Electronic Annex I), while the experiments show significant fluctuations, likely due to vibrations. The frequency spectrum at 5 m/s is matched very well by CFD at low frequencies, showing a peak at 2.4 Hz. At higher wind speeds the lower frequencies are matched reasonably but as expected higher frequencies are exhibiting amplitudes much smaller than the experiments. Sezer-Uzol and Long [15] computed the case with 15 m/s, showing fluctuations of the thrust coefficient of about 1.8%, compared with 9% of the NREL experiments and 5% in this work.

Regarding performance of the two models, there are no major differences between RANS and DES when wind velocity is small, while small but clear differences can be seen at higher velocities on time-averaged quantities. However, both models predict the same trends and magnitudes for all blade sections, indicating that these models are capable tools for wind turbine simulations, at least within the conditions simulated herein. At higher wind speeds (25 m/s), where separation is massive, DES appears to produce better results, while the opposite occurs for lower wind speeds (15 m/s). A more advanced DDES model [35] may be able to improve on these results.

4.2. Variable pitch angle for constant wind speed

Computations with variable pitch follow one of the conditions of the experimental sequence K. In this case the pitch angle is varied from -15° to 40° in increments of 5° for wind speed of 15 m/s. The resulting angles of attack at section $r/R = 0.30$ vary from 48.2 to -1.6° and at $r/R = 0.95$ vary from 34 to -16.3°. The experiments were performed for a step up, then step down procedure, while the computations were limited to the step up phase of the procedure. In the experiments there was an 8 s hold between pitch steps, while in CFD this hold was reduced to 4 s to save computational time.

Fig. 11 shows vortical structures represented by iso-surfaces of $Q = 5$, also shown in Electronic Annex IX in a blade-fixed reference system that provides greater insight of the flow field as the blade pitch angle is dynamically changed throughout the computation.

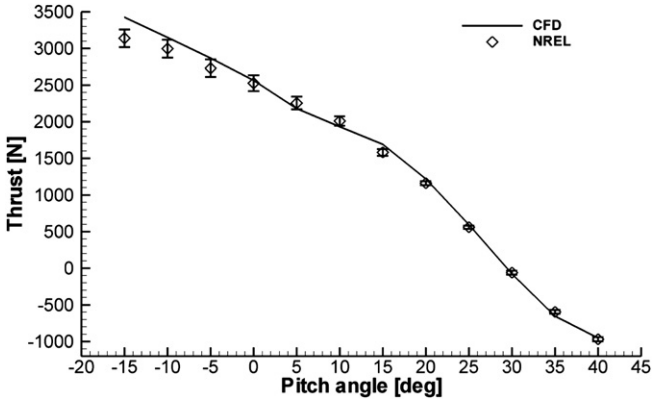

Fig. 12. Thrust for different pitch angles (wind velocity 15 m/s).

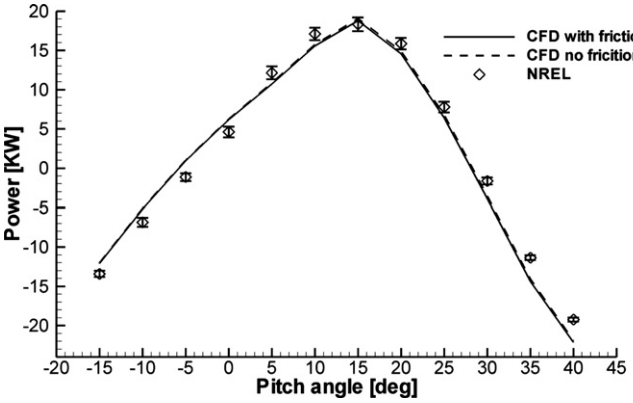

Fig. 13. Power to the shaft for different pitch angles (wind velocity 15 m/s).

At -15° of pitch the angle of attack is maximum and as expected the separation is massive. The angle of attack is zero at the tip for approximately 25° pitch, and at this condition there is a consequent absence of tip vortices. At higher pitch angles the angle of attack becomes negative and the turbine starts behaving as a fan. This can be seen in Fig. 12, which shows the thrust force on the shaft as a function of pitch angle. The thrust continuously decreases with increasing pitch angle, and is negative for pitch angles bigger than 30°. Notice the remarkably good predictions for all positive pitch angles, while the difference with the experiments increases for very large angles of attack (negative pitch angles), to reach 9% difference at -15° pitch.

The effect of pitch angle on power is shown in Fig. 13. This is an important curve since it guides the design of the controller of a pitch-controlled turbine. At wind speed of 15 m/s the maximum power predicted by CFD is 19.1 kW and occurs at 15° pitch, compared to the maximum experimental value of 18.9 kW at the same pitch angle and a rated power of 19.8 kW. At this wind speed the wind kinetic carries a potential of 160 kW, which implies a maximum mechanical efficiency of 12%. This value is particularly low because under the cited conditions the turbine is in off-design operation. At 15° pitch angle, the angle of attack is 21° at $r/R = 0.30$ and 6.6° at $r/R = 0.95$, while equal angles of attack would be achieved at wind speed of 7.5 m/s approximately. At high angles of attack CFD tends to overpredict the power, while at higher blade pitch angles (smaller and negative angles of attack) the trend reverses and the power is underpredicted. Still the ability of the code to predict this curve is remarkable.

The normal force coefficient C_n is shown in Fig. 14. The predictions are in good agreement with experiments for a wide range of sectional locations and pitch angles. Significant underpredictions occur at high

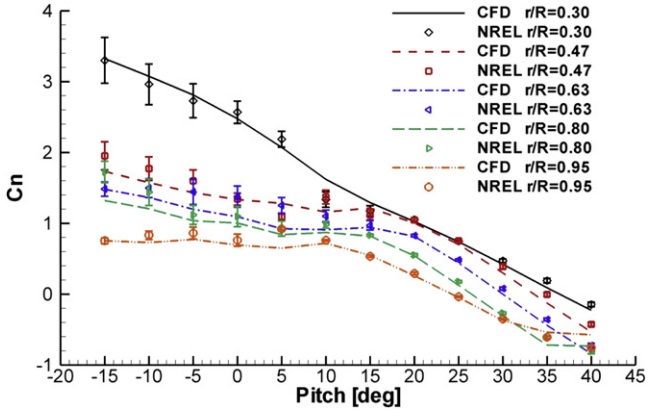

Fig. 14. Radial normal force coefficients for different pitch angles (wind velocity 15 m/s).

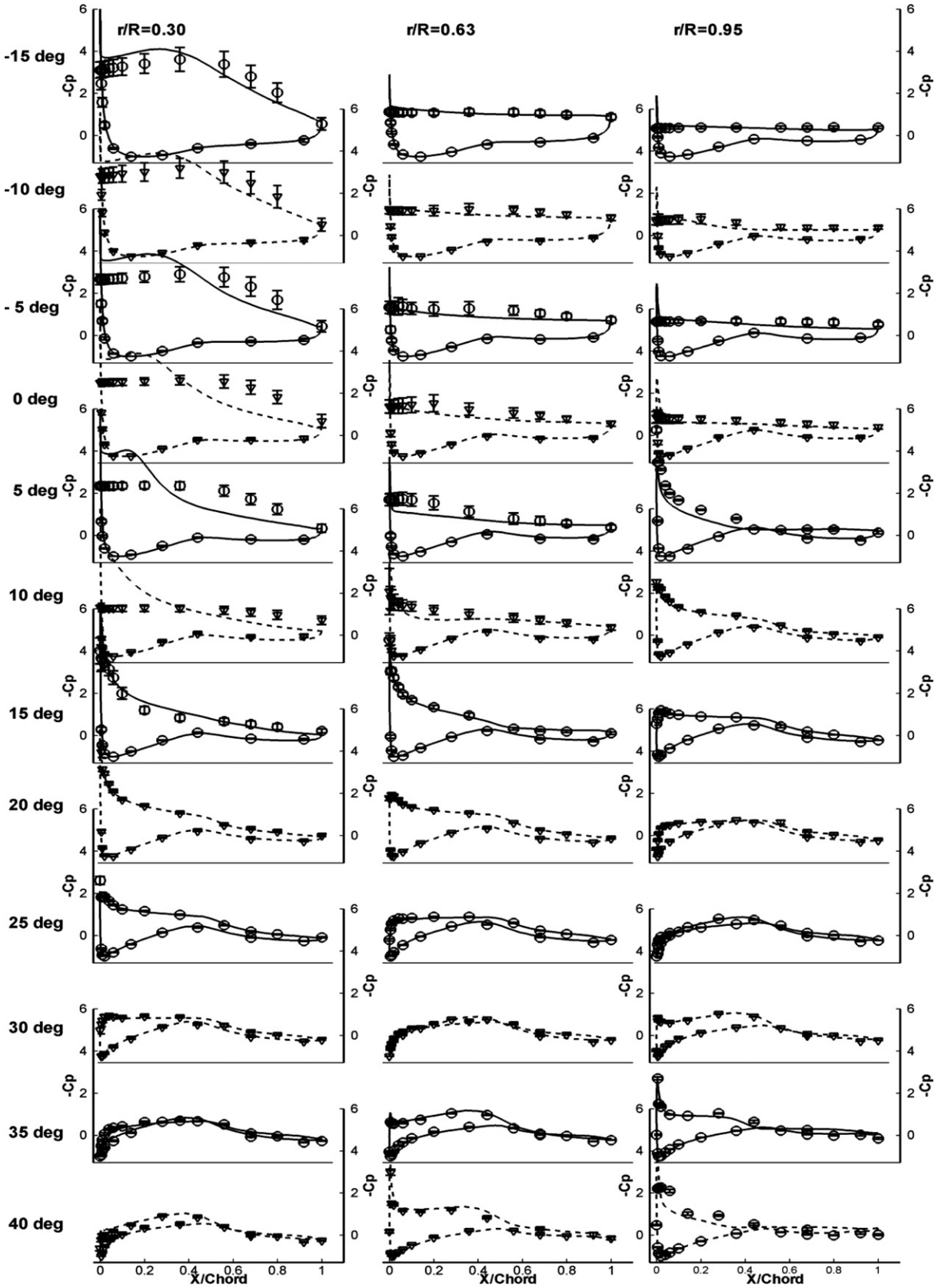

Fig. 15. Pressure coefficients at different pitch angles and blade sections (wind speed 15 m/s, lines: CFD, symbols: experiments).

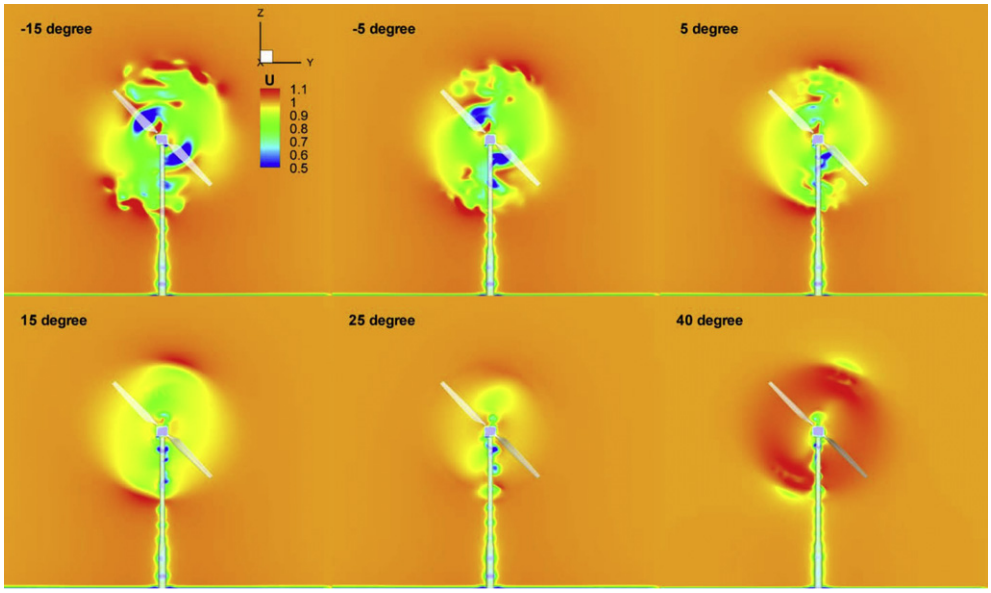

Fig. 16. Dimensionless axial velocities at $x/R = 0.8$, (wind speed 15 m/s).

angles of attack for $r/R = 0.47$ and $r/R = 0.80$, for moderate angles of attack at $r/R = 0.63$ and for low angle of attack at $r/R = 0.30$. The largest deviations are present at the innermost sections of the blade, with excellent results for $r/R = 0.80$ and $r/R = 0.95$. Notice that the normal force coefficient is, for the same blade pitch angle, mostly larger in the inner sections of the blade, consistent with a larger angle of attack in those sections. At $r/R = 0.95$, where large flow separation is observed up to about 10° of pitch (see Fig. 11), the normal force coefficient remains flat until the flow is attached, evidencing stall at large angles of attack. The essentially flat response with pitch angle occurs 5∼10° of pitch angle, and then the normal force decays faster with decreased angle of attack, becoming negative for negative angles of attack (pitch angles greater than 25° at $r/R = 0.95$ and greater than 38° at $r/R = 0.30$).

Fig. 15 shows results of pressure distributions at three blade sections for pitch angles from −15° to 40°. Predictions at $r/R = 0.95$ are excellent in trend and magnitude and are very good at $r/R = 0.63$ with some magnitude issues discussed later. In contrast, predictions at $r/R = 0.30$ are excellent in trend and magnitude for small angles of attack but fair for high angles of attack (pitch angles from −15° to 10°). At section $r/R = 0.30$ the experiments show a much flatter pressure coefficient on the suction side of the blade than the CFD predictions, mostly for 10° of blade pitch angle where the CFD and experiment discrepancies are largest. At 15° of pitch angle and higher the experiments and CFD both show attached flow and the agreement is excellent. The integral of the pressure on the normal direction, leading to the normal force coefficient of Fig. 14, is still excellent except for 10° of pitch angle, indicating that the errors in pressure tend to cancel each other at other sections, as can be seen in Fig. 14. At $r/R = 0.63$ the predicted trends are in good agreement with the data, showing stalled flow up to about 10° of pitch angle, and attached flow thereafter. The magnitude of the pressure on the suction side is a bit underpredicted for pitch angles from −5° to 10°, resulting in underpredicted normal forces as seen in Fig. 14. At section $r/R = 0.95$ the flow is stalled with flat pressure distributions on the suction side up to 0° blade pitch, and then remains mostly attached. The agreement at all angles of attack is excellent. Notice that the suction and pressure sides are reversed for negative angles of attack at all sections.

Cross-sections at $x/R = 0.8$ showing instantaneous axial velocity are depicted in Fig. 16, representing the near wakes at pitch angles −15, −5, 5, 15, 25 and 40°. The axial velocity exhibits decreases that are consistent with the level of power generated at this wind speed, shown in Fig. 13. The vortical structures evident in Fig. 11 at stall conditions (negative or small pitch angles) are present in the form of large variations of axial velocity. For instance at −15° pitch there are extensive areas with axial velocities higher than the incoming wind speed, mainly near the tip of the blade, and very low velocities for regions close to $r/R = 0.30$, but again very high wind speeds around the nacelle. On the other extreme, at 40° pitch the turbine is actually working as a fan and the axial velocities are higher than the inlet velocity.

5. Conclusions

This study presents dynamic overset CFD simulations for the NREL phase VI wind turbine. In particular, two sequences of the experiment test cases are studied with complete turbine geometry, including the NREL phase VI blades, and approximate geometries for hub, nacelle and tower. RANS and DES models are used in the simulations, and extensive comparisons with experimental data are performed. The motion model coupled with the overset methodology allows for the presence of parent/children objects, enabling the computation of variable blade pitch in a moving rotor with respect to static tower, nacelle and ground. Results at constant pitch and variable wind speed (experimental sequence S) or with constant wind speed and variable pitch (experimental sequence K) show that the CFD predictions match the experimental data consistently well, including the general trends of power and thrust, sectional normal force coefficients and pressure coefficients at different sections along the blade. At very large angles of attack the conditions are more demanding and the CFD results tend to slightly overpredict the thrust and underpredict the power. Evaluation of the transient pressure on the blades reveals that DES is able to predict fluctuations with similar frequencies to the experimental measurements; however, at least at the level of grid resolution used in this study, the amplitude is underpredicted, mainly at the outermost sections.

Future work will focus on study of off-shore wind turbines in floating structures in waves to take advantage of the air/water free surface capabilities of CFDShip-Iowa. Fluid-structure interaction of flexible blades will also be studied.

Acknowledgments

Computations were performed at the National Center for Computational Science in the Cray XT5 Jaguar, grant ARD005. Experimental results were provided by Dr. Scott Schreck, from the National Renewable Energy Laboratory at Boulder, CO. His help is deeply appreciated.

References

[1] Archer CL. Evaluation of global wind power. Journal of Geophysical Research 2005;110:D12110.
[2] GWEC Global Wind Energy Council (GWEC). Global wind 2009 report; 2009.
[3] Glauert H. Airplane propellers. In: Durand WF, editor. Aerodynamic theory. New York: Dover Publications; 1963.
[4] Shen WZ, Mikkelsen R, Sørensen JN, Bak C. Tip loss corrections for wind turbine computations. Wind Energy 2005;8:457–75.
[5] Leishman JG. A semi-empirical model for dynamic stall. Journal of the American Helicopter Society 1989;34:3–17.
[6] Langtry RB, Gola J, Menter FR. Predicting 2D airfoil and 3D wind turbine rotor performance using a transition model for general CFD codes. In: 44th AIAA aerospace sciences meeting and exhibit, Reno, Nevada, 2006.
[7] Whale J, Fisichella CJ, Selig S. Correcting inflow measurements from Hawts using a lifting-surface code. In: Proceedings 1999 ASME wind energy symposium, 1999. pp. 175–185.
[8] Hess JL. Review of integral-equation techniques for solving potential-flow problems with emphasis on the surface-source method. Computer Methods in Applied Mechanics and Engineering 1975;5:145–96.
[9] Landahl MT, Stark VJE. Numerical lifting-surface theory-problems and progress. AIAA Journal 1977;6:2049–60.
[10] Preuss RD, Morino L, Suciu EO. Unsteady potential aerodynamics of rotors with applications to horizontal-axis windmills. AIAA Journal 1980;18:385–93.
[11] Johansen J, Sørensen NN, Michelsen JA, Schreck S. Detached-eddy simulation of flow around the NREL phase VI blade. Wind Energy 2002;5:185–97.
[12] Fingersh LJ, Sinuns D, Hand M, Jager D, Cotrell J, Robinson M, et al. Wind tunnel testing of NREL's unsteady aerodynamics experiment. In: Proceedings 2001 ASME wind energy symposium, 2001. pp. 129–135.
[13] Hand MM, Simms DA, Fingersh LJ, Jager DW, Cotrell JR, Schreck S, et al. Unsteady aerodynamics experiment phase VI: wind tunnel test configurations and available data campaigns. National Renewable Energy Laboratory; 2001. NREL/TP-500–29955.
[14] Schreck S. The NREL full-scale wind tunnel experiment. Introduction to the special issue. Wind Energy 2002;5:77–84.
[15] Sezer-Uzol N, Long L., 3-D time-accurate CFD simulations of wind turbine rotor flow fields. In: 44th AIAA aerospace sciences meeting and exhibit, Reno, Nevada, 2006.
[16] Sørensen NN, Michelsen JA, Schreck S. Navier-Stokes predictions of the NREL phase VI rotor in the NASA Ames 80 ft × 120 ft wind tunnel. Wind Energy 2002;5:151–69.
[17] Duque EPN, Burklund MD, Johnson W. Navier-Stokes and comprehensive analysis performance predictions of the NREL phase VI experiment. Journal of Solar Energy Engineering 2003;125:457–67.
[18] Buning PG, Parks SJ, Chan WM, Renze KJ. Application of the chimera overlapped grid scheme to simulation of space shuttle ascent flows. In: The 4th international symposium on computational fluid dynamics, Davis, California, 1991. pp. 132–137.
[19] Potsdam MA, Mavriplis DJ. Unstructured mesh CFD aerodynamic analysis of the NREL phase VI rotor. In: 47th AIAA aerospace sciences meeting including the New Horizons Forum and aerospace exposition, Orlando, Florida, 2009.
[20] Bazilevs Y, Hsu MC, Akkerman I, Wright S, Takizawa K, Henicke B, et al. 3D simulation of wind turbine rotors at full scale. Part I: geometry modeling and aerodynamics. International Journal for Numerical Methods in Fluids; 2010. 10.1002/fld.2400.
[21] Jonkman J, Butterfield S, Musial W, Scott G. Definition of a 5-MW reference wind turbine for offshore system development. National Renewable Energy Laboratory; 2009.
[22] Huang J, Carrica PM, Stern F. Semi-coupled air/water immersed boundary approach for curvilinear dynamic overset grids with application to ship hydrodynamics. International Journal for Numerical Methods in Fluids 2008; 58:591–624.
[23] Carrica PM, Wilson RV, Stern F. An unsteady single-phase level set method for viscous free surface flows. International Journal for Numerical Methods in Fluids 2007;53:229–56.
[24] Carrica PM, Wilson RV, Noack RW, Stern F. Ship motions using single-phase level set with dynamic overset grids. Computers & Fluids 2007;36:1415–33.
[25] Noack R. SUGGAR: a general capability for moving body overset grid assembly. In: 17th AIAA computational fluid dynamics conference, Toronto, Ontario, Canada, 2005.
[26] Carrica PM, Huang J, Noack R, Kaushik D, Smith B, Stern F. Large-scale DES computations of the forward speed diffraction and pitch and heave problems for a surface combatant. Computers & Fluids 2010;39:1095–111.
[27] Paik K-J, Carrica PM, Lee D, Maki K. Strongly coupled fluid–structure interaction method for structural loads on surface ships. Ocean Engineering 2009; 36:1346–57.
[28] Menter FR. Two-equation eddy-viscosity turbulence models for engineering applications. AIAA Journal 1994;32:1598–605.
[29] Travin A, Shur M, Strelets M. Physical and numerical upgrades in the detached eddy simulation of complex turbulent flows. In: Friedrich R, Rodi W, editors. Advances in LES of complex flows; 2002. p. 239–54.
[30] Sainte-Rose B, Bertier N, Deck S, Dupoirieux F. A DES method applied to a backward facing step reactive flow. Comptes Rendus Mécanique 2009;337: 340–51.
[31] Boger DA, Dreyer JJ. Prediction of hydrodynamic forces and moments for underwater vehicles using overset grids. In: 44th AIAA aerospace sciences meeting and exhibit, AIAA 2006-1148, Reno, Nevada, 2006.
[32] Hunt JCR, Wray AA, Moin P. Eddies, stream, and convergence zones in turbulent flows. Center for Turbulence Research; 1988.
[33] Dousset V, Pothérat A. Formation mechanism of hairpin vortices in the wake of a truncated square cylinder in a duct. Journal of Fluid Mechanics 2010;653: 519–36.
[34] Simms D, Schreck S, Hand M, Fingersh LJ. NREL unsteady aerodynamics experiment in the NASA-Ames wind tunnel: a comparison of predictions to measurements. National Renewable Energy Laboratory; 2001. NREL/TP-500–29494.
[35] Shur M, Spalart P, Strelets M, Travin A. A hybrid RANS-LES approach with delayed-DES and wall-modelled LES capabilities. International Journal of Heat and Fluid Flow 2008;29:1638–49.